

Low-Threshold Plasmonic Lasers on a Single-Crystalline Epitaxial Silver Platform at Telecom Wavelength

Chien-Ju Lee,[†] Han Yeh,[†] Fei Cheng,[‡] Ping-Hsiang Su,[‡] Tsing-Hua Her,[§] Yen-Chun Chen,[†] Chun-Yuan Wang,^{||} Shangir Gwo,^{||} Seth R. Bank,[⊥] Chih-Kang Shih,^{*,‡,Ⓜ} and Wen-Hao Chang^{*,†,Ⓜ}

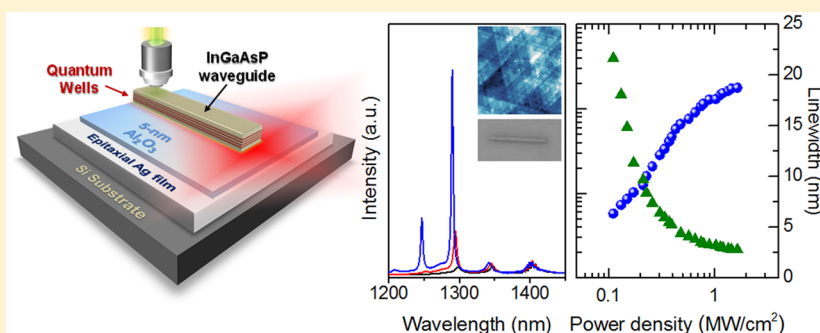
[†]Department of Electrophysics, National Chiao Tung University, Hsinchu 30010, Taiwan

[‡]Department of Physics and [⊥]Department of Electrical and Computer Engineering, The University of Texas at Austin, Austin, Texas 78712, United States

[§]Department of Physics and Optical Science, The University of North Carolina at Charlotte, Charlotte, North Carolina 28223, United States

^{||}Department of Physics, National Tsing Hua University, Hsinchu 30013, Taiwan

Supporting Information



ABSTRACT: We report on the first demonstration of metal–insulator–semiconductor-type plasmonic lasers at the telecom wavelength ($\sim 1.3 \mu\text{m}$) using top-down fabricated semiconductor waveguides on single-crystalline metallic platforms formed using epitaxially grown Ag films. The critical role of the Ag film thickness in sustaining plasmonic lasing at the telecom wavelength is investigated systematically. Low-threshold ($0.2 \text{ MW}/\text{cm}^2$) and continuous-wave operation of plasmonic lasing at cryogenic temperatures can be achieved on a 150 nm Ag platform with minimum radiation leakage into the substrate. Plasmonic lasing occurs preferentially through higher-order surface-plasmon-polariton modes, which exhibit a higher mode confinement factor, lower propagation loss, and better field–gain coupling. We observed plasmonic lasing up to $\sim 200 \text{ K}$ under pulsed excitations. The plasmonic lasers on large-area epitaxial Ag films open up a scalable platform for on-chip integrations of plasmonics and optoelectronics at the telecom wavelength.

KEYWORDS: plasmonic nanolaser, epitaxial silver film, surface plasmon polariton, semiconductor nanolaser, telecom wavelength, low threshold

Miniaturization of semiconductor lasers has been actively pursued recently not only in the quest of small device footprint, low power consumption, and high operation speed but also for the development of on-chip integration of coherent light sources.^{1,2} Conventional semiconductor lasers based on dielectric cavities have a size limited to half the effective wavelength ($\sim \lambda/2n$) in all three dimensions. In the past decade, tremendous research efforts have been directed toward cavities comprising noble metals and dielectric media, such as metal-cladded semiconductor cavities^{3–5} and structures that support surface plasmon polariton (SPP) modes,^{6–16} to achieve subdiffractional cavity size. Among these approaches, the plasmonic nanolaser or “spaser”^{17–19} is particularly attractive due to its novel concept as well as its potential to achieve a “deep subdiffraction limit”. Indeed, the plasmonic nanolaser has been successfully demonstrated in various configurations,

including metal nanosphere cavities,²⁰ metal-cladded microcavities,^{21–23} metal–insulator–semiconductor (MIS) nanowaveguides,^{6–12} and plasmonic crystals.^{24–26} The MIS structure^{6–16} has been used to achieve ultralow-threshold and continuous-wave (CW) operation of plasmonic lasers with subdiffractional confinement in all three dimensions.^{9,10} Initial concerns of high metal losses have also been mitigated by using a single-crystalline metallic platform, such as chemically synthesized Au flakes⁸ and epitaxially grown Ag^{9,10} films, on which the strong scattering and SPP damping caused by surface roughness and grain boundaries are minimized. In particular, the MIS structure based on wafer-scale and atomically smooth

Received: February 27, 2017

Published: May 16, 2017

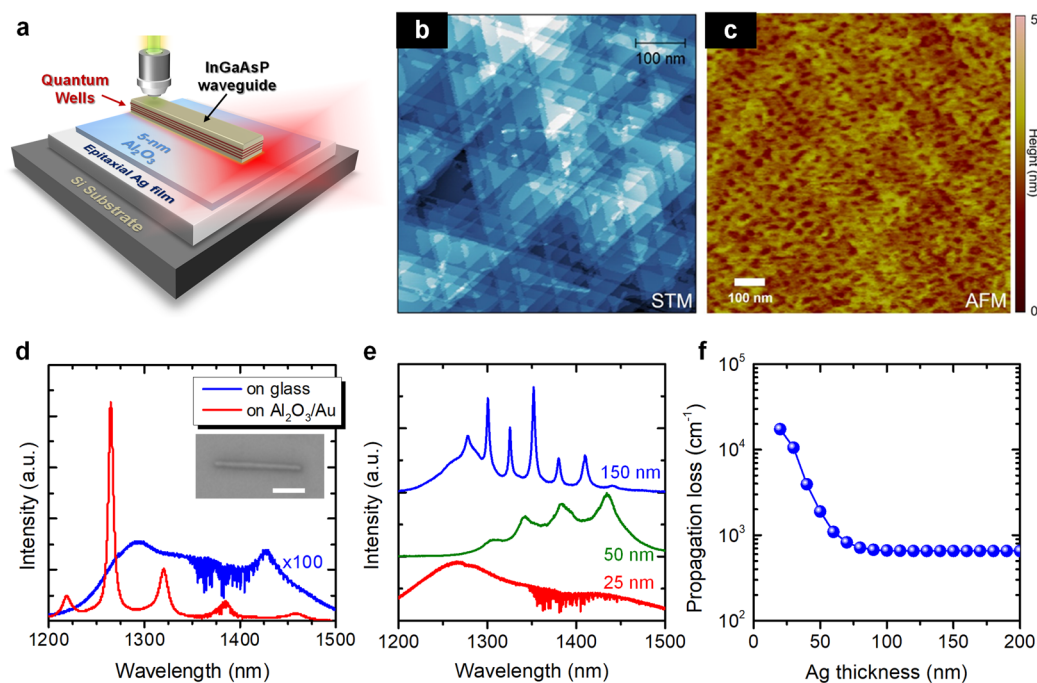


Figure 1. | Plasmonic laser structure, epitaxial Ag films, and emission spectra of SPP modes. (a) Schematic of the MIS structure. Top-down fabricated InGaAsP waveguides with embedded quantum wells were transferred onto Al_2O_3 -capped single-crystalline metallic platforms. (b) STM scan of the epitaxially grown, annealed Ag film (150 nm). (c) AFM image of the 150 nm epitaxial Ag film after Al growth and *in situ* oxidation (RMS = 0.42 nm). (d) Emission spectra of two waveguides with similar dimensions lying on glass and Au platforms, respectively. Inset: SEM image of a typical waveguide. The scale bar is 2 μm . (e) Emission spectra of waveguides on Ag platforms with Ag film thickness $t = 25, 50,$ and 150 nm. (f) Calculated propagation loss coefficient of the SPP mode in the waveguide ($\lambda = 1.3 \mu\text{m}$) as a function of Ag film thickness.

epitaxial Ag films with superior plasmonic properties opens up an unprecedented platform for the development of scalable, large-area, and monolithic integrations of plasmonics and optoelectronics.

Thus far, MIS-based plasmonic nanolasers have been demonstrated in the visible, ultraviolet, and near-infrared.^{6–16} For applications in telecom wavelengths (1.3/1.5 μm), plasmonic nanolasers have been demonstrated based on metal–insulator–metal waveguides²¹ and metal-cladded nanodisks.²² However, an MIS-based plasmonic nanolaser that facilitates on-chip integrations of plasmonics and optoelectronics at the telecom wavelength is yet to be demonstrated. Moreover, all previous demonstrations of MIS-based plasmonic nanolasers utilized bottom-up self-assembly methods to incorporate the gain media into plasmonic resonators, a process with which it is difficult (if not impossible) to create a scalable technological platform.

In this work, we report on low-threshold and CW operations of MIS-based plasmonic lasers at the telecom wavelength ($\sim 1.3 \mu\text{m}$) using InGaAsP strained quantum wells (QWs) on a single-crystalline metallic platform formed using epitaxially grown Ag films. Plasmonic waveguide lasers were fabricated by top-down approaches using electron-beam lithography followed by an all-dry transfer process (see *Methods*) to form MIS structures. Since the SPP skin depth ($1/e$ decay length) into the metal at the telecom wavelength is significantly larger than that in UV and visible regions, the critical role of Ag film thickness in preventing radiation leakage into the substrate in the MIS structure at the telecom wavelength is investigated systematically. Low-threshold and CW plasmonic lasing is demonstrated up to 125 K. At higher temperature, plasmonic lasing can be achieved under pulse excitation up to 200 K. At room temperature, only amplified spontaneous emission can be

established. The polarization of lasing SPP mode and its coupling with gain medium is discussed.

RESULTS

Plasmonic Laser Structure and SPP Resonance. Figure 1a shows a schematic of the plasmonic laser structure consisting of InGaAsP waveguides with four embedded QWs lying on top of Al_2O_3 -capped single-crystalline metallic platforms. To investigate the impact of metal film thickness, we have prepared two kinds of metallic platform in this study. The first one is an epitaxial Ag film with various thicknesses t ranging from 25 to 150 nm grown by molecular beam epitaxy (MBE) on Si substrates (see *Methods*). We have developed a new two-step procedure that can efficiently grow smooth and thick epitaxial Ag films in one growth cycle. The resulting Ag film is single crystalline with superior surface flatness, as evident from the triangular terraces shown in the scanning tunneling microscopy (STM) image of a 150 nm thick Ag film (Figure 1b). An *in situ* capping of Al_2O_3 is achieved by epitaxially growing 5 ML Al, followed by *in situ* oxidation with 10^{-6} Torr of pure oxygen for 10 min. This *in situ* Al_2O_3 capping retains the surface smoothness of the epitaxial Ag film as shown by atomic force microscopy (AFM) with a root-mean-square (RMS) roughness of 0.42 nm (Figure 1c). The high-quality Ag film thus ensures that the SPP scattering losses caused by surface roughness and polycrystalline grain boundaries can be minimized. We have also prepared a second metallic platform using chemically synthesized Au flakes²⁷ (thickness ~ 700 nm; lateral dimension ~ 100 – $200 \mu\text{m}$) dispersed on glass substrates. The thick Au film can thus be used as a reference platform for comparing SPP resonance and plasmonic lasing performance on Ag platforms. In this work, the fabricated waveguides have a

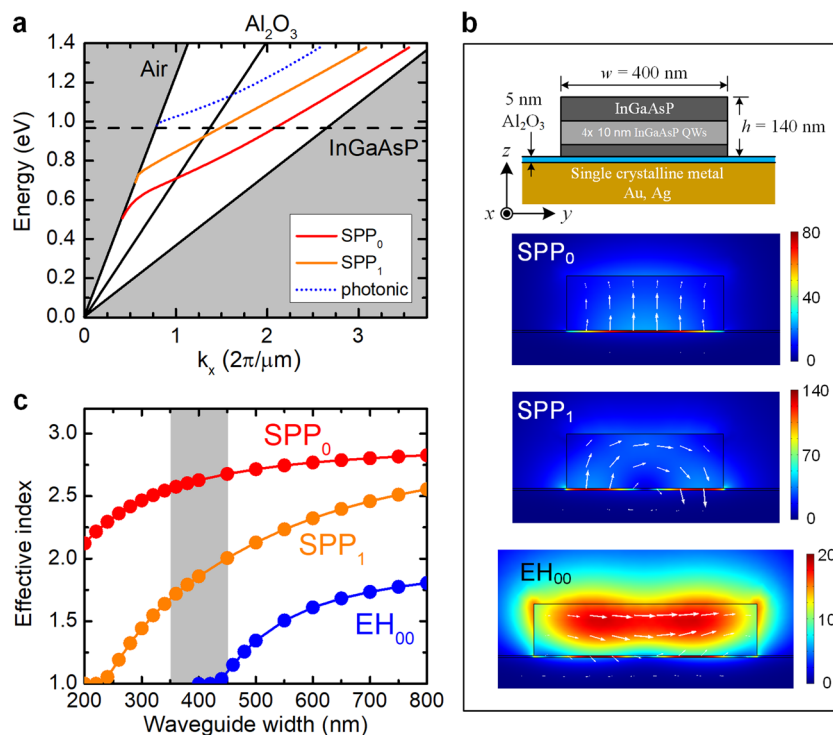


Figure 2. Dispersion relations, effective indices, and spatial confinements of SPP and photonic modes. (a) Calculated dispersion curves of waveguide modes in a plasmonic waveguide ($w = 400$ nm, $h = 140$ nm). Only the two lowest order SPP modes, SPP₀ (red) and SPP₁ (orange), can be supported in the spectral range of the QW emission band. Light lines in air and Al₂O₃ and InGaAsP bulk materials are shown by solid lines. The horizontal dashed line corresponds to a wavelength $\lambda = 1280$ nm. The lowest photonic mode EH₀₀ (blue dashed line) is cut off at $\lambda \approx 1210$ nm. (b) Schematic of the cross-section of the waveguide structure and the calculated electric field distribution $|E(x, y)|$ and direction (arrows) of SPP₀ and SPP₁ modes at $\lambda = 1280$ nm as well as the photonic EH₀₀ mode in a waveguide with $w = 600$ nm. (c) Calculated effective refractive index, n_{eff} , as a function of the waveguide width w at $\lambda = 1280$ nm.

thickness $h = 140$ nm, width $w = 300$ – 600 nm, and length $L = 3$ – 5 μm . To confirm the subwavelength confinement of SPP modes, we first examined the emission spectra of waveguides with similar dimensions ($w \approx 400$ nm, $h \approx 140$ nm, and $L \approx 5$ μm) lying on glass and on Au platforms, as shown in Figure 1d. The weak and featureless emission spectrum from the waveguide on glass indicates that waveguides of this dimension cannot support photonic modes in the QW emission band (1.2–1.5 μm). In strong contrast, clear equally spaced Fabry–Pérot (FP) modes with 2 orders of magnitude stronger PL intensity can be observed for the waveguide on Au flakes, indicative of SPP FP resonance.

We then examined the SPP FP resonance for waveguides on Ag platforms with various Ag film thicknesses t . As shown in Figure 1e, the featureless emission spectrum for $t = 25$ nm indicates that the SPP propagation on the 25 nm thick Ag film is very leaky. Increasing the Ag film thickness to $t = 50$ nm can mitigate the propagation loss, as evident from the emergence of SPP FP resonance modes in the emission spectra. For $t = 150$ nm, the line width of SPP FP resonances becomes even narrower than that on the Au platform. Although the line width is also influenced by the line width narrowing effect under optical excitations, this result suggests that the 150 nm Ag film is thick enough to prevent radiation leakage into the substrate. The calculated propagation loss in the MIS structure at 1.3 μm as a function of Ag film thickness (Figure 1f) also supports this finding.

Dispersion Relation and SPP Confinements. To gain further insight into the confined SPP modes, we calculated the dispersion relations and electric field distributions of eigen-

odes in the MIS waveguides based on the finite-element method. Figure 2a shows the dispersion relations of the lowest three eigenmodes in a waveguide with $w = 400$ nm and $h = 140$ nm on Ag spaced by a 5 nm thick Al₂O₃ layer. These eigenmodes can be classified as SPP modes or photonic modes according to their electric field distribution. As shown in Figure 2b, the SPP modes show a tightly confined electric field in the Al₂O₃ layer, while the electric fields of photonic modes are distributed mostly in the semiconductor waveguide. The SPP modes can be further characterized as SPP_{*q*} modes with the subscript q denoting the number of nodes at the metal–oxide interface along the direction perpendicular to the waveguide axis. In the spectral range of 1.2–1.5 μm , only the lowest two SPP modes (labeled as SPP₀ and SPP₁) can propagate in the plasmonic waveguide. The lowest photonic mode, characterized as the EH₀₀ mode, is cut off for wavelengths longer than 1210 nm. The dispersion curves together with the calculated effective refractive index $n_{\text{eff}}(w)$ (Figure 2c and Supporting Figure S1) can be used as a guideline to determine the optimal waveguide size. In the QW emission band, the photonic modes are cut off for waveguides with $w < \sim 450$ nm, below which only SPP modes are supported in the MIS structure. Further reduction of the waveguide width to $w < \sim 250$ nm will cut off the higher-order SPP₁ mode, leaving behind only the fundamental SPP₀ mode.

Polarization Properties and Lasing Characteristics. The SPP₀ and the SPP₁ modes can be distinguished by the polarization of waveguide emission.¹³ In the semiconductor waveguides, the electric field of the SPP₀ (SPP₁) mode is perpendicular (parallel) to the metal surface when propagating

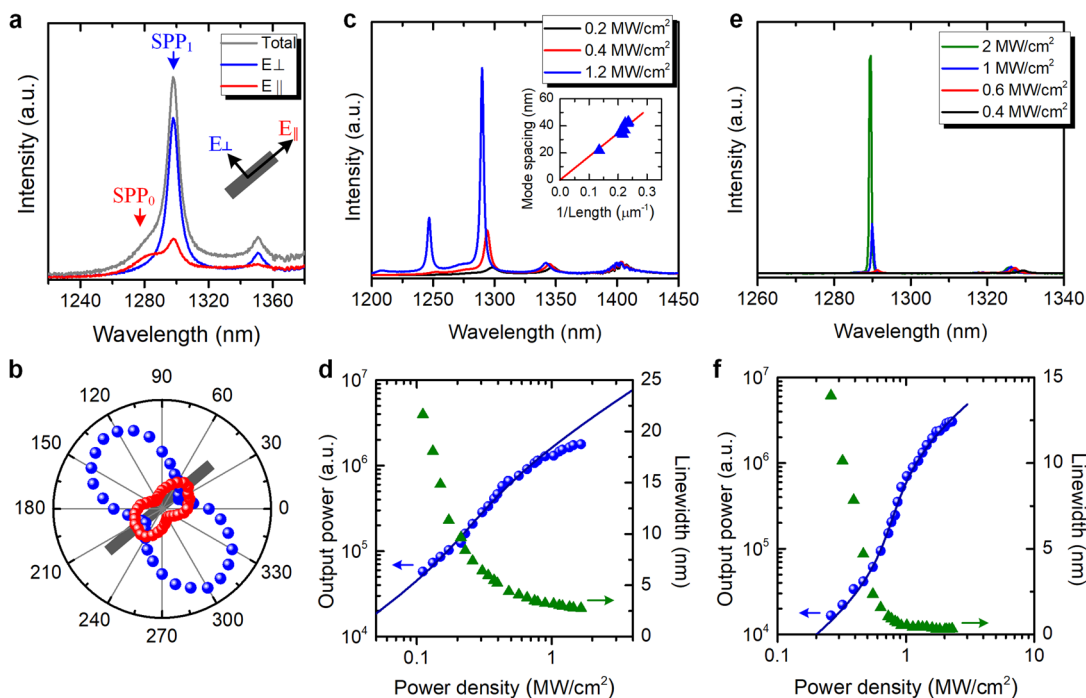


Figure 3. Polarization dependence and lasing characteristics at 4 K. (a) Polarization-resolved emission spectra of a plasmonic waveguide with polarization parallel (red curve) and perpendicular (blue curve) to the waveguide axis. (b) Polar plot of emissions from SPP₀ (red) and SPP₁ (blue) modes. The gray bar indicates the waveguide axis. (c) Lasing spectra of a waveguide with $w = 380$ nm and $L = 4.8$ μm . Inset: Measured cavity mode spacing (blue dots) as a function of the inverse waveguide length. A linear fit suggests a group index of $n_g = 4.8$. (d) L–L curve (blue circle) and the line width narrowing (green circle) of the lasing peak at 1280 nm shown in (c). The lasing threshold is 0.2 MW/cm². (e) Photonic lasing spectra for a wider waveguide with $w = 500$ nm. (f) L–L curve and the line width narrowing of the photonic lasing peak at 1290 nm shown in (e). Solid lines in (d) and (f) are fitting curves using the rate equation model. The obtained β factors are $\beta = 0.25$ for plasmonic lasing (d) and $\beta = 0.02$ for photonic lasing (f).

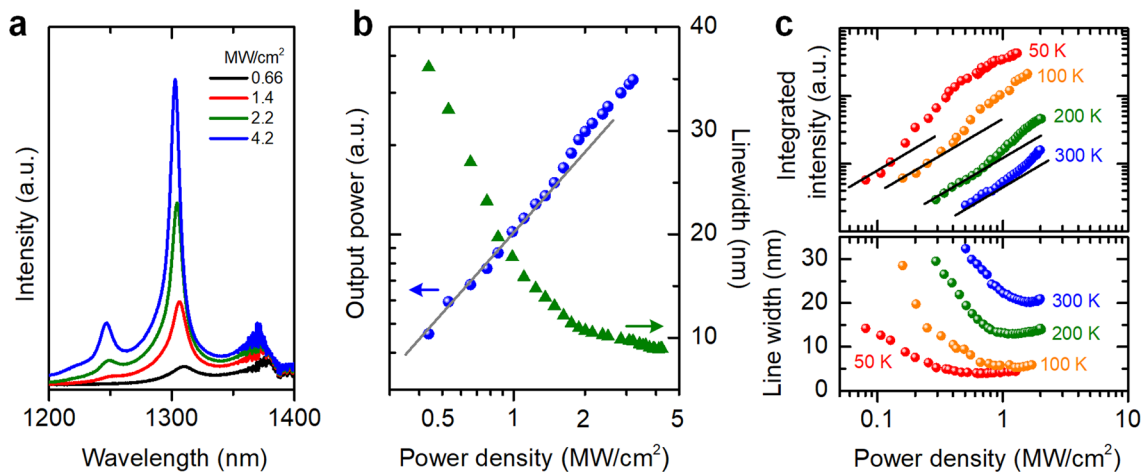


Figure 4. Temperature dependence of plasmonic lasing. (a) Emission spectra of a waveguide at $T = 125$ K under CW pumping at different power densities. (b) L–L curve (blue circles) and the line width narrowing (green triangles) of the lasing peak near 1300 nm shown in (a). The lasing threshold is ~ 1.4 MW/cm². (c) L–L curves (upper panel) and line width narrowing (lower panel) for a waveguide under pulsed laser excitations at various temperatures.

along the waveguide axis (see arrows in Figure 2b). As a result, the polarization of the scattered field by the end facets is parallel (perpendicular) to the waveguide axis for the SPP₀ (SPP₁) mode.^{9,13} Figure 3a and b show the polarization-resolved emission spectra of the confined SPP modes in a waveguide with $w \approx 400$ nm, where the SPP₀ and SPP₁ modes can be clearly distinguished. For the waveguide dimension investigated here, the SPP₁ mode always shows a narrower line width and stronger intensity compared with the SPP₀ mode.

This can be understood from the polarization selection rule of the gain medium. Since the QW emission is dominantly TE polarized (i.e., electric field along the QW plane) and the QW plane is parallel to the metal surface, the coupling of QWs to the SPP₀ mode with the electric field perpendicular to the metal surface is prohibited. This explains why most of the optical gain couples preferentially to the SPP₁ mode as observed in the polarization-resolved measurements. In this regard, further reduction of the waveguide width to support only the SPP₀

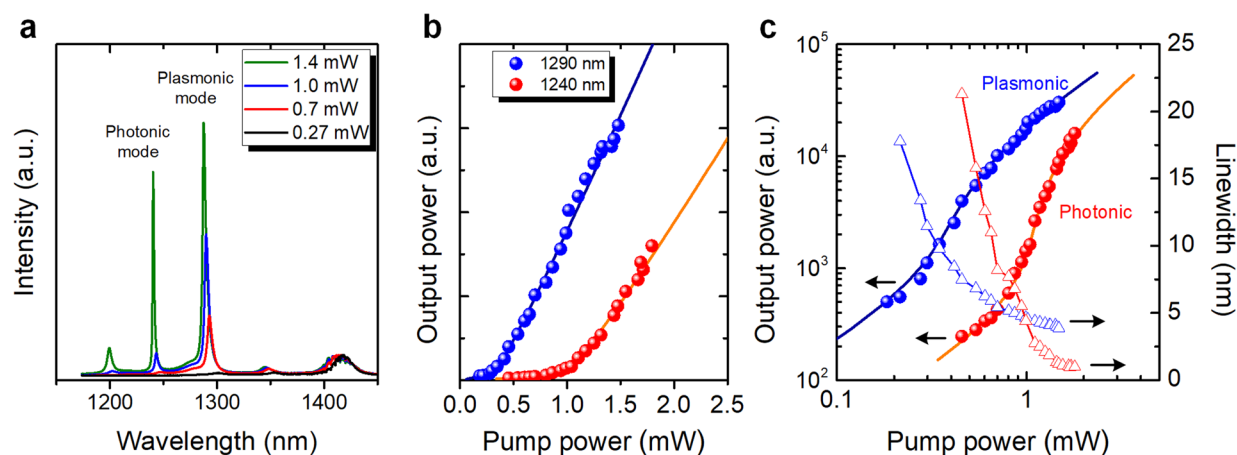


Figure 5. Plasmonic and photonic dual-mode lasing. (a) Emission spectra of a waveguide with $w = 410$ nm at 4 K under pulsed pumping at different powers. (b) L–L curve of the plasmonic lasing at 1290 nm (blue circles) and photonic lasing at 1240 nm (red circles). (c) L–L curves in log–log scale (solid symbols) and line width narrowing (open symbols) of the plasmonic (blue) and photonic (red) lasing. Solid lines in (b) and (c) are fitting curves using the rate equation model. The obtained β factors are $\beta = 0.1$ and $\beta = 0.025$ for plasmonic and photonic lasing, respectively.

mode is unfavorable for plasmonic lasing due to the polarization mismatch between the SPP_0 mode and the QW gain medium. According to the calculated $n_{\text{eff}}(w)$, the optimal waveguide width for plasmonic lasers is in the range of $w \approx 350$ – 450 nm, in which the SPP_1 mode is well confined, while the photonic modes are cut off in order to ensure plasmonic lasing.

Figure 3c shows the emission spectra of a waveguide ($w = 380$ nm) at 4 K under quasi-CW excitation (see Methods) at different power densities. Longitudinal SPP FP modes resonating between the waveguide end-facets are observed. With increasing pumping density, the spectral blue-shift, line width narrowing, and sharp increase in output intensity of the peak near $1.3 \mu\text{m}$ indicate plasmonic lasing oscillation. The S-shaped light-out versus light-in (L–L) curve of the lasing peak in log–log scale clearly shows a transition from spontaneous emission to amplified spontaneous emission and eventually to full lasing oscillations. From a rate-equation-model fitting, a lasing threshold of $0.2 \text{ MW}/\text{cm}^2$ and a spontaneous-emission coupling factor $\beta \approx 0.25$ are determined. Compared with the lasing threshold of $\sim 20 \text{ MW}/\text{cm}^2$ for the MIS-based plasmonic lasers on nonepitaxial metal films in the visible range,⁶ the threshold of our plasmonic lasers on epitaxial Ag films is about 2 order of magnitude smaller at low temperatures. For waveguides with $w > 500$ nm, the lasing characteristic turns to photonic lasing instead of plasmonic lasing (Figure 3e,f). The lasing characteristics of plasmonic and photonic lasers can be distinguished by the lasing line width and the β factor. The typical lasing line width of plasmonic lasers is 2–5 nm, significantly larger than the photonic lasing line width of ~ 0.2 – 1 nm, due to the lower propagation loss of the photonic mode. In addition, the plasmonic laser typically has a larger β factor due to the stronger field–gain coupling. The extracted β factor for photonic lasing is in the range of $\beta = 0.01$ – 0.03 , which is much smaller than that of the plasmonic laser with $\beta = 0.1$ – 0.3 (Supporting Figure S3).

Temperature Dependence of Lasing Characteristics.

To examine the performance of our plasmonic lasers at higher temperatures, we increase the operation temperature from 4 K to room temperature. Under CW pumping, we observed plasmonic lasing up to 125 K (Figure 4a,b), albeit at a higher lasing threshold ($\sim 1.5 \text{ MW}/\text{cm}^2$). In addition, the maximum

lasing temperature is significantly higher than that on Au flakes (~ 50 K). This can be attributed to the superior plasmonic properties of the epitaxial Ag film at the telecom wavelength and the reduced heat accumulation in the waveguides due to the improved heat dissipation efficiency through the large-area Ag film on a Si substrate, in comparison with Au flakes (~ 100 – $200 \mu\text{m}$) on a glass substrate. We have also examined the lasing performance under pulsed laser excitations (400 ps/40 MHz). As shown in Figure 4c, pulsed plasmonic lasing is clearly sustained to 200 K. At room temperature (300 K), the signature of the line width narrowing and nonlinear power dependence are also observed. However, they are more likely corresponding to the signatures of amplified spontaneous emission before the full lasing oscillation, primarily limited by the maximum available power of our excitation laser.

Distinction between Plasmonic and Photonic Lasing Modes. How to substantiate plasmonic lasing is an important issue especially when both plasmonic and photonic modes coexist in the MIS waveguide structures. This issue was often addressed, as we have shown previously, by shrinking the device dimensions such that all photonic modes are cut off in the waveguide. However, it becomes ambiguous when device dimensions are around (or not much smaller than) the cutoff size of the photonic modes, where photonic lasing may be triggered and could be misinterpreted as plasmonic lasing. In order to clearly distinguish plasmonic versus photonic lasing, we have specifically designed a device structure where both plasmonic and photonic modes can be supported. The device is a waveguide with a dimension ($w \approx 410$ nm) that is at the border of the photonic mode cutoff. The calculated cutoff wavelength of photonic modes is around ~ 1250 nm (Supporting Figure S2), which is very close to the typical lasing wavelength at ~ 1300 nm. As shown in Figure 5, both plasmonic and photonic lasing can be observed in the waveguide under pulsed pumping. The plasmonic lasing occurs at 1290 nm with a low threshold ~ 0.3 mW, whereas photonic lasing occurs at 1240 nm with a higher threshold of ~ 1.0 mW. This higher lasing threshold and the lower output power of the photonic mode are indicative of its higher modal loss due to the poor modal confinement. From the L–L curves in log–log scale and the line width narrowing with increasing pumping power (Figure 5c), it becomes clear that plasmonic lasing

shows a broader lasing line width and exhibits a less pronounced “kink” feature near the threshold. The former can be attributed to the higher dissipative loss and the latter to the stronger electromagnetic field confinement of the SPP modes, which gives rise to a higher β factor. Since both plasmonic and photonic modes in this waveguide lase through the same gain material, the dual-mode lasing thus unambiguously clarifies the very distinct lasing behaviors of plasmonic and photonic modes.

DISCUSSION

Here we discuss the factors that impact the highest operation temperature of the plasmonic laser. Thus far, our MIS waveguide structure has not yet allowed us to achieve full plasmonic lasing at room temperature in the telecom wavelength. The high mirror reflection loss and the increased nonradiative recombination considerably hinder plasmonic lasing operations at high temperatures. According to rate-equation-model fittings to the lasing characteristics, the deduced cavity photon decay rate corresponds to a total modal loss coefficient of about $\alpha_T \approx 8000 \text{ cm}^{-1}$. In the MIS waveguide structure, the modal loss comprises the metal absorption loss α_M , the scattering loss α_S , and the radiation loss α_R . The radiation loss arises predominantly from mirror reflection loss, $\alpha_R = -(1/L) \ln R$, where L is the waveguide length and R is the average reflectivity at the waveguide end facets. The reflectivity R can be estimated to be $|n_{\text{eff}} - 1| / (n_{\text{eff}} + 1)^2 \approx 8.2\%$, where $n_{\text{eff}} \approx 1.8$ is the effective index of the SPP₁ mode in the waveguide with $w \approx 400 \text{ nm}$. The corresponding mirror reflection loss for waveguide length $L = 3\text{--}5 \mu\text{m}$ is about $\alpha_R \approx 5011\text{--}8352 \text{ cm}^{-1}$, which is already comparable with the estimated total modal loss α_T , indicating that the end-facet reflection is the dominating loss channel in the waveguide structure. This is particularly true for our waveguides formed by wet chemical etching, where the end facets are less well-defined as compared with cleaved facets of nanorods or nanowires.^{6,9,11–15} Indeed, according to the material parameters from Johnson and Christy's data,²⁸ the estimated metal absorption loss for a Ag film at the telecom wavelength is about $\alpha_M \approx 650 \text{ cm}^{-1}$. The metal absorption loss and the scattering loss caused by metal surface roughness have been suppressed by the use of an epitaxial Ag film. However, we noted the lasing threshold at low temperature is still significantly higher than that of nanolasers based on InGaN/GaN core-shell nanorods on epitaxial Ag films,^{9,10} where a larger β factor ($\beta \approx 0.73$) and a significant gain enhancement due to the high group index ($n_g \approx 9$) caused by the gain-medium-loading effect have been reported. For the plasmonic waveguides in this study, the group index deduced from the longitudinal mode spacing is $n_g \approx 4.8$ (inset in Figure 3b), which is very close to the calculated group index of the SPP₁ mode ($n_g = 4.9$) in a bare waveguide without the gain-medium-loading effect. Further optimizing the spectral matching between the gain medium ($\sim 1.4 \mu\text{m}$) and the lasing mode ($\sim 1.3 \mu\text{m}$) to take advantages of gain enhancement by the slowing down of group velocity may further reduce the plasmonic lasing threshold at low temperature.

Room-temperature MIS-based plasmonic lasers have been reported on nonepitaxial metal films in visible and UV ranges,^{7,11,12} but with very high lasing thresholds in the range of a few $\sim \text{GW}/\text{cm}^2$ (peak pump intensity). While our MIS waveguides have not yet achieved full plasmonic lasing at room temperature within the limitation our excitation laser, the onset

of amplified spontaneous emission at $\sim 1.4 \text{ MW}/\text{cm}^2$ (time-averaged power) corresponds to a very low peak pump intensity of $\sim 87 \text{ MW}/\text{cm}^2$ in comparison with those in the $\sim \text{GW}/\text{cm}^2$ range.

On the other hand, we noted that the emission intensity decreases substantially with increasing temperature (Figure 4c), which can be attributed to the increased nonradiative recombination rate and hence significant gain reduction at elevated temperatures. The nonradiative recombination is attributed to the surface recombination caused by fabrication-induced defects at the etched sidewalls. The increased metal absorption losses and reduced gain caused by more pronounced nonradiative recombination at elevated temperatures thus substantially limit the operation temperature of our plasmonic waveguide lasers. To achieve plasmonic lasing at higher temperatures, subwavelength microrings or microdisks that supports whispering-gallery SPP modes without mirror reflection loss can reduce the modal loss considerably. The fabrication-induced nonradiative recombination can also be mitigated by suitable surface passivations. We believe that the wafer-scale and atomically smooth epitaxial Ag platform with superior plasmonic properties is very promising to realize room-temperature plasmonic lasers at the telecom wavelength for scalable, large-area, and monolithic on-chip integration of plasmonics with optoelectronics.

METHODS

Fabrication of MIS Structures. The plasmonic laser devices consist of semiconductor waveguides lying on top of Al_2O_3 -capped single-crystalline metallic platforms formed using either chemically synthesized Au flakes or an epitaxially grown Ag film. The chemically synthesized Au flakes have a typical thickness in the range of $0.7\text{--}1.2 \mu\text{m}$, with a lateral dimension of $\sim 100\text{--}200 \mu\text{m}$ and a smooth surface with a typical RMS roughness less than 1 nm (Supporting Figure S5). The 5 nm thick Al_2O_3 capping layer was deposited by atomic layer deposition. The waveguides were fabricated from an epitaxial InGaAsP structure on an InP substrate containing four layers of 1.2% compressively strained QWs as the gain medium.²⁹ The four QWs have a well width of 10 nm , separated by 15 nm barrier layers. InGaAsP waveguides were fabricated using electron-beam lithography followed by wet chemical etching using HBr-based solution. The resulting InGaAsP waveguides on top of the InP sacrificial layer have a width in the range of $300\text{--}600 \text{ nm}$ and length in the range of $3\text{--}5 \mu\text{m}$. The distance from the bottommost QW to the bottom surface of the waveguide layer is 15 nm . Then the fabricated waveguides were transferred onto the surface of metallic platforms using an all-dry transfer process with polydimethylsiloxane (PDMS) films.³⁰ The sample containing waveguides was first upside down attached to a PDMS film. Then, a selective wet-etching process using HCl solution was utilized to remove the InP sacrificial layer underneath the InGaAsP waveguide layer. Once the sacrificial layer was completely removed, the waveguides attaching on the PDMS film can be lifted up from the substrate. The transfer process is carried out under an optical microscope. The PDMS film with attached waveguides was mounted on a three-axis translational stage and gradually brought into contact with the surface of the metallic platforms. In this way, the fabricated waveguides can be positioned precisely at desired locations. By slowly peeling off the PDMS film, the waveguides can be detached from the PDMS film and

transferred onto the metallic platform, forming the MIS structure.

Epitaxial Growth of Ag Films. Successful development of epitaxial growth of an atomically smooth, single-crystalline Ag film had played a central role in the realization of ultralow-threshold nanolasing in the visible range.⁹ The growth procedure reported previously, however, is rather complicated and time-consuming. In particular, the low growth rate, the lengthy annealing process, and the requirement of several growth cycles to achieve the desired film thickness all make it challenging to grow much thicker films (>150 nm) for nanolasing applications at the telecom wavelength. To overcome such a difficulty, we have developed a new two-step procedure combining a high-rate growth and a high-temperature-anneal process, which enables us to grow smooth epitaxial Ag films in one growth cycle. In addition, an *in situ* passivation using an ultrathin aluminum oxide (~2 nm) layer is also developed to protect the Ag films for subsequent processes. The result pertinent to plasmonic lasing in the telecom wavelength is discussed here, although technical details of this new growth method will be reported elsewhere. As shown in Figure 1b, the STM image of a 150 nm thick epitaxial film exhibits triangular terraces. A fluctuation of 5 ML is typically observed for a film thickness of >150 nm (~600 ML). The *in situ* capping is achieved by first growing a 5 ML epitaxial layer of Al, which is lattice matched to the Ag film, followed by oxidizing *in situ* in the load lock with high purity oxygen (99.999%) for 10 min at 1.5×10^{-6} Torr. This procedure leads to a densified, uniform aluminum oxide (AlO_x). This *in situ* oxidation of Al is superior to previously reported capping methods, where a low-band-gap semiconductor material, such as germanium (Ge), was employed. The AFM image of the 150 nm thick Ag film after Al growth and *in situ* oxidation (Figure 1c) presents a smooth surface with an RMS roughness of ~0.42 nm. X-ray diffraction analysis also confirms that the epitaxial Ag film is single crystalline without residual Al on top of the Ag film after *in situ* oxidation of the capping Al. After the Ag film growth and *in situ* oxidization, we further deposited an *ex situ* capping layer of 3 nm of aluminum oxide by atomic layer deposition, resulting in an aluminum oxide layer with a total thickness of ~5 nm on the Ag film for plasmonic studies.

Optical Measurements. The optical emissions from the fabricated waveguides were measured by a microphotoluminescence (μ -PL) setup integrated in a cryogen-free cryostat (Attocube) at a base temperature of about ~3.8 K. The samples were mounted on a low-temperature three-axis piezostage for precise positioning of the target waveguide with the excitation laser spot. The waveguides were pumped by a TTL-modulated 785 nm diode laser operating in quasi-CW mode with a 10 kHz repetition rate and a 1 μ s pulse duration (duty cycle = 0.01). The excitation powers referred to in this work are the peak power of the excitation pulse duration. An aspheric lens with a numerical aperture of 0.5 was used for focusing the laser beam. The pumping spot of about ~5 μ m in diameter ensures that each waveguide was illuminated completely. The emission signals were collected by the same lens and analyzed by a 0.5 m spectrometer using a liquid-nitrogen-cooled InGaAs diode array. For pulsed excitation measurements, the excitation source was replaced by a 635 nm picosecond pulsed diode laser (PicoQuant LDH-P-635) with a 40 MHz repetition rate and a pulse duration of ~400 ps. The referenced excitation power is the time-averaged power.

Numerical Simulations. The finite-element method was used to investigate the waveguide mode properties of the MIS structures. A 2D mode analysis was performed to find eigenmodes of the hybrid waveguide structure and calculate the complex effective indices of each transverse waveguide modes.³¹ The propagation loss of each mode was calculated from the imaginary part of the effective index. The confinement factor Γ_0 was calculated as the ratio of the electric energy in the QW regions and the total electric energy of the mode. Perfectly matched layers were used to simulate the open boundary conditions. The dielectric constants of Au and Ag at telecom wavelengths were obtained from the Johnson and Christy data.²⁸

Rate Equation Model Fitting. A simplified rate equation model considering the photon density s and exciton density n with a pumping rate p is used to analyze the lasing behavior:^{6,13,32}

$$\frac{dn}{dt} = \eta p - An - \Gamma As(n - n_0) - A_{nr}n$$

$$\frac{ds}{dt} = \beta An + \Gamma As(n - n_0) - \gamma s$$

where n_0 is the exciton density at transparency,³³ γ is the cavity photon decay rate, η is the pump photon to exciton conversion efficiency, β is the spontaneous emission factor, A and A_{nr} are the radiative and nonradiative recombination rates of excitons, and $\Gamma = (n_g/n_{eff})\Gamma_0$ is the effective confinement factor, where $\Gamma_0 \approx 0.21$ is the mode overlap between the SPP₁ mode and the QW region according to finite-element simulations (Supporting Figure S1). The exciton radiative recombination rate is given by $A = FA_0$, where F is the Purcell factor and A_0 is the spontaneous emission rate into free space modes. For simplicity, we assume $A_0 = (1 \text{ ns})^{-1}$ and $F = 1$. The main fitting parameters are the spontaneous emission factor β and the cavity photon decay rate γ , which is the sum of propagation loss and mirror reflection loss of the plasmonic waveguide. The monomolecular rate constant, A_{nr} , is further included to account for the increased nonradiative recombination in the gain medium at high temperatures.³⁴ The nonradiative recombination rate A_{nr} is assumed to be zero at 4 K.³⁵

■ ASSOCIATED CONTENT

📄 Supporting Information

The Supporting Information is available free of charge on the ACS Publications website at DOI: 10.1021/acsp Photonics.7b00184.

The confinement factors and propagation losses; effective indices of the waveguide with $w = 410$ nm; β factor and lasing line width for the MIS waveguide lasers; optical images of lasing output; optical microscope image and AFM analysis of Au flakes (PDF)

■ AUTHOR INFORMATION

Corresponding Authors

*E-mail: shih@physics.utexas.edu.

*E-mail: whchang@mail.nctu.edu.tw.

ORCID

Chih-Kang Shih: 0000-0003-2734-7023

Wen-Hao Chang: 0000-0003-4880-6006

Author Contributions

W.H.C. and C.J.L. conceived the idea and designed the experiment. C.J.L. performed the spectroscopy measurements. The epitaxial silver films were grown and characterized by F.C., P.H.S., S.B., and C.K.S. The devices were fabricated by C.J.L., H.Y., C.Y.W., and S.G. Numerical simulations and modeling were performed by C.J.L. and assisted by T.H.H. and Y.C.C. C.J.L., W.H.C., and C.K.S. wrote the paper. All authors discussed the results and commented on the manuscript.

Notes

The authors declare no competing financial interest.

ACKNOWLEDGMENTS

This work was supported by the Ministry of Science and Technology of Taiwan (MOST-104-2628-M-009-002-MY3, MOST-105-2119-M-009-014-MY3), AOARD (FA2386-16-1-4035), the National Science Foundation (NSF-DMR-1306878, NSF-ECCS-1408302), and the Welch Foundation (F-1672). W.H.C. acknowledges the support from the Center for Interdisciplinary Science of NCTU.

REFERENCES

- (1) Gwo, S.; Shih, C.-K. Semiconductor Plasmonic Nanolasers: Current Status and Perspectives. *Rep. Prog. Phys.* **2016**, *79*, 086501.
- (2) Hill, M. T.; Gather, M. C. Advances in Small Lasers. *Nat. Photonics* **2014**, *8*, 908–918.
- (3) Hill, M. T.; Oei, Y.-S.; Smalbrugge, B.; Zhu, Y.; de Vries, T.; van Veldhoven, P. J.; van Otten, F. W. M.; Eijkemans, T. J.; Turkiewicz, J. P.; de Warrdt, H.; et al. Lasing in Metallic-Coated Nanocavities. *Nat. Photonics* **2007**, *1*, 589–594.
- (4) Nezhad, M. P.; Simic, A.; Bondarenko, O.; Slutsky, B.; Mizrahi, A.; Feng, L. A.; Lomakin, V.; Fainman, Y. Room Temperature Subwavelength Metallo-Dielectric Lasers. *Nat. Photonics* **2010**, *4*, 395–399.
- (5) Khajavikhan, M.; Simic, A.; Katz, M.; Lee, J. H.; Slutsky, B.; Mizrahi, A.; Lomakin, V.; Fainman, Y. Thresholdless Nanoscale Coaxial Lasers. *Nature* **2012**, *482*, 204–207.
- (6) Oulton, R. F.; Sorger, V. J.; Zentgraf, T.; Ma, R.-M.; Gladden, C.; Dai, L.; Bartal, G.; Zhang, X. Plasmon Lasers at Deep Subwavelength Scale. *Nature* **2009**, *461*, 629–632.
- (7) Ma, R. M.; Oulton, R. F.; Sorger, V. J.; Bartal, G.; Zhang, X. Room-Temperature Sub-Diffraction-Limited Plasmon Laser by Total Internal Reflection. *Nat. Mater.* **2011**, *10*, 110–113.
- (8) Wu, C.-Y.; Kuo, C.-T.; Wang, C.-Y.; He, C.-L.; Lin, M.-H.; Ahn, H.; Gwo, S. Plasmonic Green Nanolaser Based on a Metal-Oxide-Semiconductor Structure. *Nano Lett.* **2011**, *11*, 4256–4260.
- (9) Lu, Y.-J.; Kim, J.; Chen, H.-Y.; Wu, C.; Dabidian, N.; Sanders, C. E.; Wang, C.-Y.; Lu, M. Y.; Li, B.-H.; Qiu, X.; et al. Plasmonic Nanolaser Using Epitaxially Grown Silver Film. *Science* **2012**, *337*, 450–453.
- (10) Lu, Y.-J.; Wang, C.-Y.; Kim, J.; Chen, H.-Y.; Lu, M.-Y.; Chen, Y.-C.; Chang, W.-H.; Chen, L.-J.; Stockman, M. I.; Shih, C.-K.; et al. All-Color Plasmonic Nanolasers with Ultralow Thresholds: Autotuning Mechanism for Single-Mode Lasing. *Nano Lett.* **2014**, *14*, 4381–4388.
- (11) Sidiropoulos, T. P. H.; Roder, R.; Geburt, S.; Hess, O.; Maier, S. A.; Ronning, C.; Oulton, R. F. Ultrafast Plasmonic Nanowire Lasers near the Surface Plasmon Frequency. *Nat. Phys.* **2014**, *10*, 870–876.
- (12) Zhang, Q.; Li, G. Y.; Liu, X. F.; Qian, F.; Li, Y.; Sum, T. C.; Lieber, C. M.; Xiong, Q. H. A Room Temperature Low-Threshold Ultraviolet Plasmonic Nanolaser. *Nat. Commun.* **2014**, *5*, 4953.
- (13) Ho, J.; Tatebayashi, J.; Sergeant, S.; Fong, C. F.; Iwamoto, S.; Arakawa, Y. Low-Threshold Near-Infrared GaAs–AlGaAs Core–Shell Nanowire Plasmon Laser. *ACS Photonics* **2015**, *2*, 165–171.
- (14) Chou, Y.-H.; Chou, B.-T.; Chiang, C.-K.; Lai, Y.-Y.; Yang, C.-T.; Li, H.; Lin, T.-R.; Lin, C.-C.; Kuo, H.-C.; Wang, S.-C.; Lu, T.-C.

Ultrastrong Mode Confinement in ZnO Surface Plasmon Nanolasers. *ACS Nano* **2015**, *9*, 3978–3983.

(15) Chou, Y.-H.; Wu, Y.-M.; Hong, K.-B.; Chou, B.-T.; Shih, J.-H.; Chung, Y.-C.; Chen, P.-Y.; Lin, T.-R.; Lin, C.-C.; Lin, S.-D.; Lu, T.-C. High-Operation-Temperature Plasmonic Nanolasers on Single-Crystalline Aluminum. *Nano Lett.* **2016**, *16*, 3179–3186.

(16) Liu, N.; Gocalinska, A.; Justice, J.; Gity, F.; Povey, I.; McCarthy, B.; Pemble, M.; Pelucchi, E.; Wei, H.; Silien, C.; Xu, H.; Corbett, B. Lithographically Defined, Room Temperature Low Threshold Subwavelength Red-Emitting Hybrid Plasmonic Lasers. *Nano Lett.* **2016**, *16*, 7822–7828.

(17) Bergman, D. J.; Stockman, M. I. Surface Plasmon Amplification by Stimulated Emission of Radiation: Quantum Generation of Coherent Surface Plasmons in Nanosystems. *Phys. Rev. Lett.* **2003**, *90*, 027402.

(18) Stockman, M. I. Spasers explained. *Nat. Photonics* **2008**, *2*, 327–329.

(19) Stockman, M. I. The spaser as a nanoscale quantum generator and ultrafast amplifier. *J. Opt.* **2010**, *12*, 024004.

(20) Noginov, M. A.; Zhu, G.; Belgrave, A. M.; Bakker, R.; Shalae, V. M.; Narimanov, E. E.; Stout, S.; Herz, E.; Suteewong, T.; Wiesner, U. Demonstration of a spaser-based nanolaser. *Nature* **2009**, *460*, 1110–1112.

(21) Hill, M. T.; Marell, M.; Leong, E. S. P.; Smalbrugge, B.; Zhu, Y.; Sun, M.; van Veldhoven, P. J.; Geluk, E. J.; Karouta, F.; Oei, Y.-S.; et al. Lasing in Metal-Insulator-Metal Sub-Wavelength Plasmonic Waveguides. *Opt. Express* **2009**, *17*, 11107–11112.

(22) Kwon, S.-H.; Kang, J.-H.; Seassal, C.; Kim, S.-K.; Regreny, P.; Lee, Y.-H.; Lieber, C. M.; Park, H.-G. Subwavelength Plasmonic Lasing from a Semiconductor Nanodisk with Silver Nanoparticle Cavity. *Nano Lett.* **2010**, *10*, 3679–3683.

(23) Ding, K.; Ning, C. Z. Metallic Subwavelength-Cavity Semiconductor Nanolasers. *Light: Sci. Appl.* **2012**, *1*, e20.

(24) van Beijnum, F.; van Veldhoven, P. J.; Geluk, E. J.; de Dood, M. J. A.; 't Hooft, G. W.; van Exter, M. P. Surface Plasmon Lasing Observed in Metal Hole Arrays. *Phys. Rev. Lett.* **2013**, *110*, 206802.

(25) Zhou, W.; Dridi, M.; Suh, J. Y.; Kim, C. H.; Co, D. T.; Wasielewski, M. R.; Schatz, G. C.; Odom, T. W. Lasing Action in Strongly Coupled Plasmonic Nanocavity Arrays. *Nat. Nanotechnol.* **2013**, *8*, 506–511.

(26) Yang, A.; Hoang, T. B.; Dridi, M.; Deeb, C.; Mikkelsen, M. H.; Schatz, G. C.; Odom, T. W. Real-Time Tunable Lasing from Plasmonic Nanocavity Arrays. *Nat. Commun.* **2015**, *6*, 6939.

(27) Huang, J.-S.; Callegari, V.; Geisler, P.; Bruning, C.; Kern, J.; Prangma, J. C.; Wu, X.; Feichtner, T.; Ziegler, J.; Weinmann, P.; et al. Atomically Flat Single-Crystalline Gold Nanostructures for Plasmonic Nanocircuitry. *Nat. Commun.* **2010**, *1*, 150.

(28) Johnson, P. B.; Christy, R. W. Optical Constants of the Noble Metals. *Phys. Rev. B* **1972**, *6*, 4370–4379.

(29) Lu, T.-W.; Lee, P.-T.; Tseng, C.-C.; Tsai, Y.-Y. Modal Properties and Thermal Behaviors of High Quality Factor Quasi-Photonic Crystal Microcavity with Different Central Post Sizes. *Opt. Express* **2008**, *16*, 12591–12598.

(30) Castellanos-Gomez, A.; Buscema, M.; Molenaar, R.; Singh, V.; Janssen, L.; van der Zant, H. S. J.; Steele, G. A. Deterministic Transfer of Two-Dimensional Materials by All-Dry Viscoelastic Stamping. *2D Mater.* **2014**, *1*, 011002.

(31) Oulton, R. F.; Sorger, V. J.; Genov, D. A.; Pile, D. F. P.; Zhang, X. A Hybrid Plasmonic Waveguide for Subwavelength Confinement and Long Range Propagation. *Nat. Photonics* **2008**, *2*, 496–500.

(32) Coldren, L. A.; Corzine, S. W. *Diode Lasers and Photonic Integrated Circuits*; Wiley: New York, 1995.

(33) Park, H.-G.; Kim, S.-H.; Seo, M.-K.; Ju, Y.-G.; Kim, S.-B.; Lee, Y.-H. Characteristics of Electrically Driven Two-Dimensional Photonic Crystal Lasers. *IEEE J. Quantum Electron.* **2005**, *41*, 1131–1141.

(34) Sweeney, S. J.; Phillips, A. F.; Adams, A. R.; O'Reilly, E. P.; Thijs, P. J. A. The Effect of Temperature Dependent Processes on the Performance of 1.5- μm Compressively Strained InGaAs(P) MQW

Semiconductor Diode Lasers. *IEEE Photonics Technol. Lett.* **1998**, *10*, 1076–1078.

(35) Fehse, R.; Tomić, S.; Adams, A. R.; Sweeney, S. J.; O'Reilly, E. P.; Andreev, A.; Riechert, H. A Quantitative Study of Radiative, Auger, and Defect Related Recombination Processes in 1.3- μm GaInNAs-Based Quantum-Well Lasers. *IEEE J. Sel. Top. Quantum Electron.* **2002**, *8*, 801–810.